

Role of Silicon as Structural Stabilizer and Redox-Active Element in Multicomponent (Sn, Sb, Fe, Si) Alloy Electrodes for Na-Ion Batteries

Yuliia Kravets, Yanan Sun, Hui Wang, and Philipp Adelhelm*

Metal alloys are attractive electrode materials for sodium-ion batteries (SIBs) thanks to their high theoretical capacities. Because of its good availability and promising use in Li-ion batteries, silicon is also interesting for SIBs. However, so far its use has not been very successful because formation of the NaSi phase (954 mAh g^{-1}) is kinetically unfavorable. Here, the role of Si in multicomponent alloys composed of redox-active metals tin (Sn), antimony (Sb), and redox-inactive iron (Fe) is investigated. The composites are prepared by high-energy ball milling. The resulting particles and agglomerates are typically in the lower μm range ($0.5\text{--}10 \mu\text{m}$) and contain, depending on the composition, the different metals and

the intermetallic phases SnSb, FeSn, FeSn₂, FeSi and FeSi₂. It is found that Si remains electrochemically inactive irrespective of its chemical state, but still provides some benefits. Similar to Fe, Si acts as a structural stabilizer for composite electrodes. Excellent rate capability is demonstrated by the Sn:Si:Fe alloy, while the highest capacity and long-term stability are found for the Sn:Sb:Si (2:2:1) alloy. The stabilizing effect of Si (and Fe) is observed through operando electrochemical dilatometry, which shows a much smaller degree of electrode breathing compared to the Si/Fe-free electrode.

1. Introduction

Sodium-ion batteries (SIBs) are currently being investigated as a promising low-cost alternative to lithium-ion batteries (LIBs). While both technologies are based on very similar electrochemistry, sodium is a much more abundant and widespread resource.^[1–7] Although a complete replacement of LIBs with SIBs is unlikely due to the lower energy density of the latter, much effort has been devoted to the design of SIBs for more specific fields of application.^[8,9] Investigations into various SIB anode materials, both those that were already tested in LIBs and new ones, have included carbon-based compounds, alloying anodes, metal oxides, and more.^[10–14]

Alloying anodes for SIBs have garnered much attention due to their high gravimetric and volumetric theoretical capacities and low operating voltages.^[15–17] Among these, Si has been the focus of many studies due to its high theoretical capacity (954 mAh g^{-1} for NaSi) and promising results in the Li-ion system.^[18] Despite

the existence of this intermetallic (IM) phase, the alloying process of bulk Si and Na is more complex. Most experimental attempts to obtain the NaSi phase through electrochemical cycling have proved unsuccessful likely due to the high activation energy of Na diffusion into crystalline Si.^[19–21] Contrary to this, Si in its amorphous phase facilitates the diffusion of Na ions.^[15] This indicates that crystallinity is a major factor influencing the diffusion kinetics in the Na–Si system. Following this finding, various techniques have been used in attempts to activate Si for use in SIBs. However, although favorable results have been reported in literature, for example, for Si incorporated into C-matrices^[22] and MXene structures^[23] or for Si thin films,^[24] it is quite challenging to prove whether or to what degree Si has really become redox-active. This is because other factors, such as the carbon additive^[25] or the host structure, can also contribute to the reported capacity values. To the best of our knowledge, the redox activity of Si has never been convincingly demonstrated, for example, by X-ray diffraction (XRD) analysis or by observing voltage profiles that would be typical for alloy formation.

Much more promising results compared to Si are typically obtained for Sn and Sb, with redox potentials around 0.2 V and 0.6 versus Na^+/Na and theoretical capacities of 847 and 660 mAh g^{-1} for $\text{Na}_{15}\text{Sn}_4$ and Na_3Sb , respectively.^[15] In addition to these favorable properties, Sn is also nontoxic and environmentally friendly. However, the use of bare Sn or Sb as anode materials leads to poor cycling stability due to the large volume increase of the alloying process ($\approx 420\%$ for Sn and 390% for Sb).^[26] This generally causes cracking and pulverization of the electrode material, resulting in loss of electrical contact and hence capacity fading over time. To minimize or limit these detrimental processes and their effects, different strategies have been investigated. These include synthesizing composites of Sn or Sb with various amounts

Y. Kravets, Y. Sun, H. Wang, P. Adelhelm
Institut für Chemie

Humboldt-Universität zu Berlin
Brook-Taylor-Str. 2, 12489 Berlin, Germany
E-mail: philipp.adelhelm@hu-berlin.de

Y. Sun, P. Adelhelm
Helmholtz-Zentrum Berlin für Materialien und Energie GmbH
Research Group Operando Battery Analysis (CE-GOBA)
Hahn-Meitner-Platz 1, 14109 Berlin, Germany

 Supporting information for this article is available on the WWW under <https://doi.org/10.1002/batt.202400690>

 © 2025 The Author(s). *Batteries & Supercaps* published by Wiley-VCH GmbH. This is an open access article under the terms of the Creative Commons Attribution License, which permits use, distribution and reproduction in any medium, provided the original work is properly cited.

of carbon,^[27,28] use of IMs and alloys including SnSb,^[29–31] Sb–Si and Sn–Si,^[32,33] Sn₄P₃,^[34,35] and others.^[36,37] Moreover, different particle morphologies,^[38,39] binders,^[40,41] and electrolytes are being used.^[27,42] Progress in alloying anode materials for Na-ion batteries has recently been summarized.^[5,26,43,44]

A general finding from previous studies is that the electrochemical properties of IMs are more favorable than those of the individual elements. An obvious example is the comparison of Sn and the IMs Sn_{0.51}Sb_{0.49} (SnSb for brevity). While a stepped voltage profile is observed for Sn due to a series of complex phase transformations, the SnSb shows a much more sloping behavior.^[29,45] With a theoretical capacity of 754 mAh g⁻¹, SnSb has also been the focus of various studies to improve its long-term cycling, many of which revolve around reducing the alloy SnSb particle size and designing different carbon-based networks.^[46–51] Other approaches include creating porous metal frameworks around the particles to act as robust matrices to alleviate the effects of volume changes^[52–54] or using synthesis methods such as electrodeposition, sputtering, or ball milling to control the distribution and size of metal particles.^[55–58]

Other multielement alloy compositions containing both electrochemically active and inactive elements have also been investigated. Comprising various combinations of elements such as Sn, Sb, Bi, Ge, and Fe, many of these compounds demonstrate improved performance in terms of capacity retention, rate capability, or both.^[59–61] In particular, the addition of the electrochemically inactive Fe has been of interest with its intended use of creating a matrix that is both highly conductive and capable of buffering unwanted volume changes during sodiation/desodiation.^[62–64] The general viability of using multicomponent alloys in batteries was demonstrated by Sony in 2005 Corp. with the release of the NEXELION battery, a Li-ion battery with an anode

comprised of nanometer-sized Sn–Co grains surrounded by a carbon matrix.^[65] While it demonstrated favorable performance, the presence of Co in the composition significantly drove up the price of the battery, leading to partial substitution of the element with Fe over the years.^[66]

In this work, we investigate the role of Si as a member of multicomponent alloys and the influence it has on the electrode capacity and lifetime of SIBs. The alloys with selected compositions in the Sn–Sb–Fe system are prepared by high-energy planetary ball milling. The overarching idea is to investigate whether Si can be electrochemically active in such composites due to the thorough mixing of the elements or by the formation of silicon-containing intermetallic phases in the mixture. The morphology and the structure of the composites are studied with scanning electron microscopy (SEM) and XRD. Electrochemical studies are performed in half-cells with Na as the counter electrode and using an ether-based electrolyte (1 M NaPF₆ in diglyme). The ether-based electrolyte was chosen because it generally allows better electrode stability of metal anodes compared to the more common carbonate electrolytes.^[27,42,67] Electrode expansion/shrinkage (“breathing”) is studied by operando electrochemical dilatometry (ECD).

2. Results and Discussion

2.1. Synthesis and Alloy Compositions

To investigate the specific influence of alloying different elements on the electrochemical performance, both binary and multielement alloys with elements such as Sn, Sb, Si, and Fe were synthesized.

Figure 1 provides a general overview of the material synthesis and half-cell assembly process. The sample naming convention

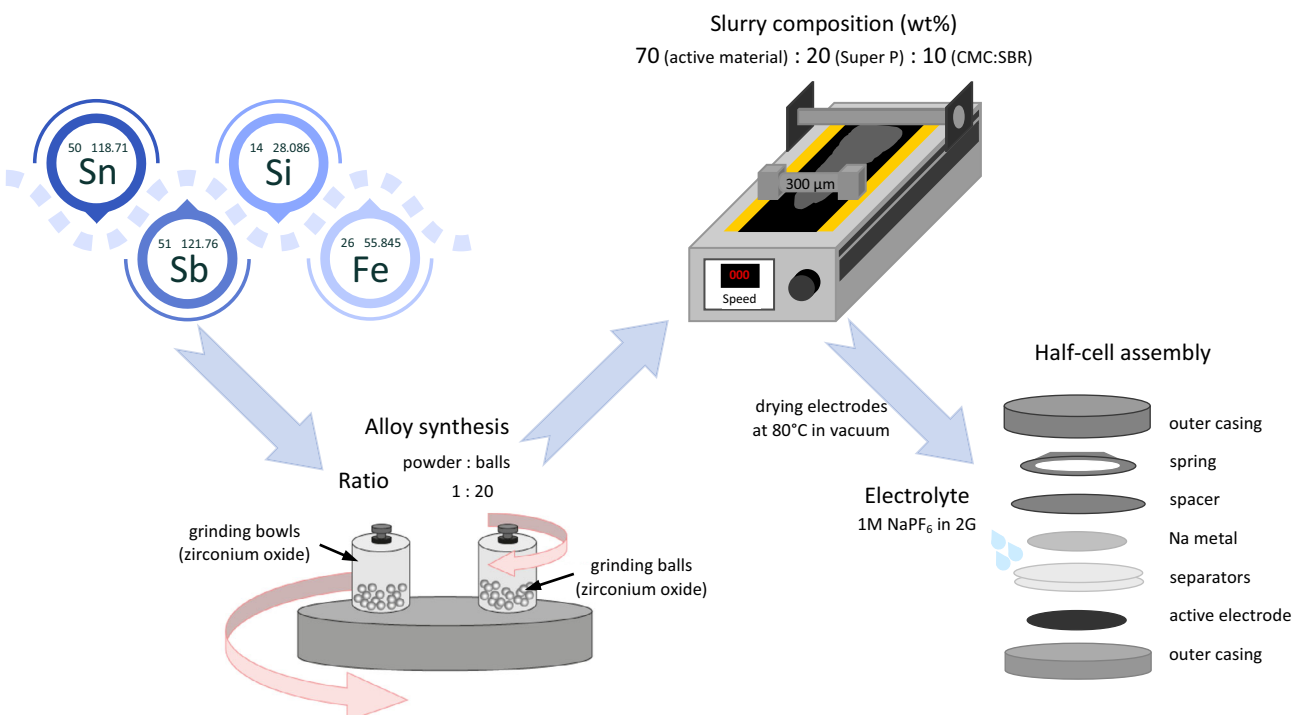


Figure 1. Schematic of the elemental composition, electrode synthesis process, and half-cell assembly.

begins with Sn and Sb, as these elements are always electrochemically active during cycling, followed by Si, whose activity is to be determined. For simplicity, only materials with equal mass ratios between the different elements in the composition were selected. It follows that a sample such as the Sn:Sb would always be synthesized with a 1:1 mass ratio of Sn and Sb. The same naming principle was applied to subsequent multielement alloys, that is, the Sn:Sb:Si:Fe alloy was composed of a 1:1:1:1 mass ratio of all the elements contained. This rule also made the calculation of theoretical capacities for any given sample straightforward.

An overview of the theoretical specific capacities of the synthesized materials is given in **Table 1**. The table contains values for both cases of Si being either electrochemically active or inactive. Fe is inactive, so the higher its content, the lower the theoretical capacity. In an attempt to maximize the theoretical capacity value, the Sn:Sb:Si sample was the only one synthesized with a 2:2:1 mass ratio in addition to 1:1:1, resulting in a theoretical capacity value of 603 mAh g⁻¹ with 80 wt% SnSb in the overall composition.

For the electrochemical experiments, all theoretical capacities were calculated assuming that only Sn and Sb are redox-active and that Si (and other elements) are redox-inactive, see Table 1. If the experiments show capacity values significantly exceeding the theoretical capacity, then Si is likely to be redox-active. Note that excess capacity during initial sodiation can also be caused by solid electrolyte interphase (SEI) formation. The conductive additive can also contribute to excess capacity.^[68]

It should be noted that samples containing Sn:Sb:Fe were also tested; however, their results were inferior compared to all other alloys and were difficult to reproduce. Results are therefore not discussed. One reason for the poor performance of these alloys could be related to the complicated phase composition of the electrodes, as both Sn and Sb form multiple IM compounds with Fe, see **Table 2**.

2.2. Structure and Morphology

SEM was used to study the morphology of the synthesized alloyed samples, see **Figure 2a–f**. The particles and agglomerates are typically between 0.5 and 10 µm in diameter and show various shapes as expected from the ball milling synthesis. In a few cases, larger particles were also observed. Attempts to reduce the particle size failed due to the low melting temperature of Sn (232 °C),^[49] which results in larger particles in cases of intense milling. At the other extreme, previous experiments have shown that short ball milling times and low rotational frequencies lead to powder mixing rather than the formation of alloys such as SnSb.^[29] Therefore, achieving the optimum particle size

Table 2. Possible binary IMs between the elements investigated. IMs in bold were found in the samples of this study. To the best of our knowledge, no ternary compounds have been reported so far.^[61]

	Sb	Si	Fe
Sn	Sn_{0.51}Sb_{0.49}, Sb₃Sn₄ ^[73]	No IMs ^[74]	Fe ₅ Sn ₃ , Fe ₃ Sn ₂ , FeSn, FeSn₂ ^[75]
Sb		No IMs ^[76]	FeSb, FeSb ₂ ^[77,78]
Si			Fe ₂ Si, Fe ₅ Si ₃ , FeSi, FeSi₂ ^[78,79]

through ball milling is a balancing act between the rotational frequency and duration of the synthesis. Further reduction in particle size is not necessarily desirable, as nanomaterials also have inherent drawbacks.^[39] Size-related advantages proposed for micro-sized materials include higher mass loadings at given electrode thicknesses leading to higher volumetric energy densities; lower surface area reducing the initial capacity loss occurring during the first cycle; and easier fabrication, industrial production scaling, and subsequent cost reduction compared to the hurdles required to synthesize many high-quality nanomaterials.

The presence of a large amount of fine Si particles in the Sn:Si sample can be understood if no IMs are formed between Sn and Si during the synthesis process, so that ball milling merely acts as a method of mixing the two materials. To a lesser extent, this can also be noticed for the Sn:Sb:Si sample, in line with the expectation that Si does not alloy with Sn or Sb. Samples containing Fe in general exhibit smaller particle sizes when compared to an alloy such as SnSb. This is most likely caused by the very different melting temperatures of the individual components (i.e., 1538 °C for Fe^[64] and 232 and 630.6 °C for Sn and Sb, respectively^[49]). The high temperatures reached during the energy-intensive ball milling processes not only assist in overcoming the activation energy barrier to the formation of intermetallics but also lead to subsequent particle growth and agglomeration. For this reason, the smaller particle size for the Fe-containing samples seems reasonable, as the higher melting temperatures counteract particle growth compared to the other compositions.

Powder XRD patterns of the as-synthesized alloys are depicted in **Figure 2g,h**, divided according to the electrochemically active elements present in the overall composition without the influence of Si. Several reference patterns are included to assign the phases formed. As mentioned above, **Table 2** provides a summary of IMs reported in the literature that may be formed by the combination of the selected elements. **Figure 2g** shows the results for the Sn-containing samples Sn:Fe, Sn:Si, Sn:Si:Fe. Except for the Sn:Fe, crystalline β-Sn can be clearly identified. **Figure 2h** provides results for various compositions containing Sn and Sb. For all these samples, crystalline Sn_{0.51}Sb_{0.49}

Table 1. Theoretical capacities of the compositions studied, assuming that Sn and Sb are redox-active (formation of Na₁₅Sn₄ and Na₃Sb), that Fe is redox-inactive, and that Si is either redox-inactive or active (formation of NaSi).

Alloy composition mass ratio	Sn	Sb	Sn:Sb 1:1	Sn:Si 1:1	Sn:Fe 1:1	Sn:Si:Fe 1:1:1	Sn:Sb:Si 1:1:1	Sn:Sb:Si 2:2:1	Sn:Sb:Si:Fe 1:1:1:1
Theoretical capacity w/o Si [mAh g ⁻¹]	847	660	754	423	423	282	502	603	376
Theoretical capacity w Si [mAh g ⁻¹]	n.a.	n.a.	n.a.	900	n.a.	600	820	793	615

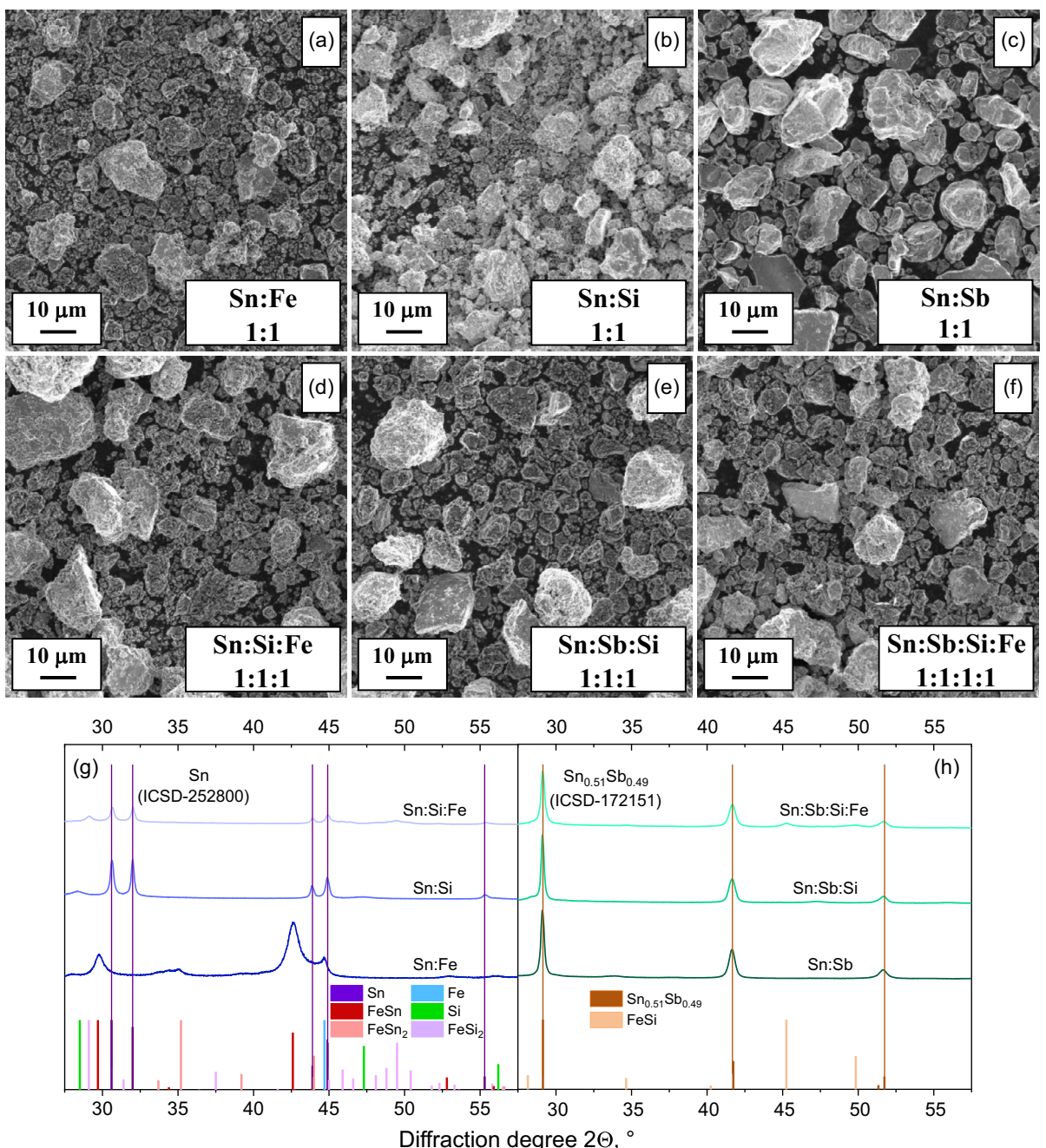


Figure 2. a-f) SEM images of the synthesized samples. g,h) X-ray powder diffraction patterns of Sn-based (Sn:Fe, Sn:Si, and Sn:Si:Fe) and SnSb-based (Sn:Sb, Sn:Sb:Si, and Sn:Sb:Si:Fe) compositions. Vertical lines represent the reference patterns for Sn (ICSD-252800) and $\text{Sn}_{0.51}\text{Sb}_{0.49}$ (ICSD-172151) as indicated in the graph legends. Other phases have been identified to be Fe (ICSD-48382), Si (ICSD-257794), FeSn (ICSD-150620), Fe Sn_2 (ICSD-199316), Fe Si_2 (ICSD-9119), and Fe Si (ICSD-41997).

(ICSD-172151) is well visible, indicating that Sn and Sb readily form an IM. A closer look at the sample consisting only of Sn and Fe shows that FeSn (hexagonal, P6₃/mmc, ICSD-150620) and Fe Sn_2 (tetragonal, I4/mcm, ICSD-199316) are formed during synthesis. On the other hand, the presence of Si does not seem to exert influence on the patterns for either Sn- or SnSb-based compositions. This is in line with information inferred from SEM images for these materials in Figure 2a-f, as no IMs are formed between Sn or Sb and Si. However, this behavior is not the case for alloys containing both Si and Fe. As evident in Figure 2g,h, the

IMs formed include $\text{Sn}_{0.51}\text{Sb}_{0.49}$, Fe Si (cubic, P2₁3, ICSD-41997), and Fe Si_2 (orthorhombic, Cmca, ICSD-9119), indicating that Fe preferentially alloys with Si rather than Sn or Sb. Notably, none of the XRD patterns show evidence of crystalline Si, hinting at amorphization, especially for the Fe-free samples.

The amorphous nature of Si in the compositions was also evidenced by Raman spectroscopy, see Supporting Information, Figure S2. While bulk crystalline Si demonstrates a clear Raman band around 520 cm^{-1} , the ball-milled composites show broadening and shifting of the band to lower wavenumbers. A broader

signal with a maximum between 485 and 495 cm⁻¹ has been linked to amorphous Si by previous studies.^[69,70] As mentioned above, amorphous Si has been suggested to be electrochemically active, which therefore should lead to a notable increase in the capacity of electrodes.

2.3. Electrochemical Properties: Na Storage Capacity

Properties of the electrodes were investigated by galvanostatic cycling. The voltage profiles of different alloys for the 1st and 200th cycles are shown in Figure 3a,b (Sn-containing alloys) and c,d (Sn- and Sb-containing alloys). The highest capacity is obtained for the binary SnSb electrode. The first discharge capacity of 706 mAh g⁻¹ is in agreement with previous reports and the theoretical capacity of 754 mAh g⁻¹ and supports that both elements are redox-active and operate at full capacity. In contrast, the capacity is lower for the binary electrodes Sn:Si and especially Sn:Fe. For the Sn:Si electrode, the first discharge capacity amounts to 331 mAh g⁻¹. This is well below what would be expected in case all Sn (423 mAh g⁻¹) or both Sn and Si (900 mAh g⁻¹) were active. After 200 cycles, the electrode delivers 77% of its initial capacity. This indicates that the Si, despite being XRD amorphous, is not able to store Na ions. The fact that only Sn is redox-active is supported by the voltage profile, which shows a typical stepped behavior known for Sn.^[29,71]

The Sn:Fe electrode shows an initial capacity of only 92 mAh g⁻¹, which is again well below what would be expected if Sn were fully active (423 mAh g⁻¹). As Fe and Sn form various IMs (see Table 1), the decrease indicates that Sn chemically bound to Fe is largely electrochemically deactivated. In fact, assuming

the formation of FeSn₂ (see XRD results in Figure 2b), all Sn in the composite would be bound to Fe. This is also supported by the voltage profile, which lacks most of the typical step-like behavior typical of Sn. Note that the sloping voltage profile may also be partly caused by the carbon additive.

The behavior of the ternary Sn:Si:Fe electrode is intermediate and again shows a lot of similarity to the voltage profile of pure Sn.^[71] The obtained first capacity of 277 mAh g⁻¹ almost equals the theoretical value of 282 mAh g⁻¹ (assuming that only Sn is active), indicating that no IMs are formed with Sn and that Si is not redox-active. These findings are consistent with the XRD results, which show that Si preferentially alloys with Fe rather than Sn. In fact, the formation of FeSi₂ would bind all the Si and Fe of the sample in the IM (the Si/Fe molar ratio in the sample is 1.99), leaving all the Sn available to store Na. The almost complete utilization of Sn in this sample indicates that the composite approach benefits the electrochemical activity.

Voltage profiles in Figure 3c,d show that the addition of Sb to the composites changes the voltage profile and achievable specific capacities. With Sb as an additional redox-active element, the achievable storage capacities increase, and the multistep voltage profile typical of Sn changes to a profile with two large plateaus which become less defined over cycling. Although the initial capacity of 706 mAh g⁻¹ is close to the theoretical one, strong fading occurs with prolonged cycling, reaching around 462 mAh g⁻¹, or 65%, after 200 cycles. The capacities obtained for the ternary and quaternary SnSb:Si and Sn:Sb:Si:Fe are, as expected, lower, providing 508 and 397 mAh g⁻¹, respectively, during the first sodiation. These values are close to theoretical ones, assuming that only Sn and Sb are redox-active (502 and 376 mAh g⁻¹). The minor excess capacity of the Sn:Sb:Si:Fe alloy upon first discharge is most

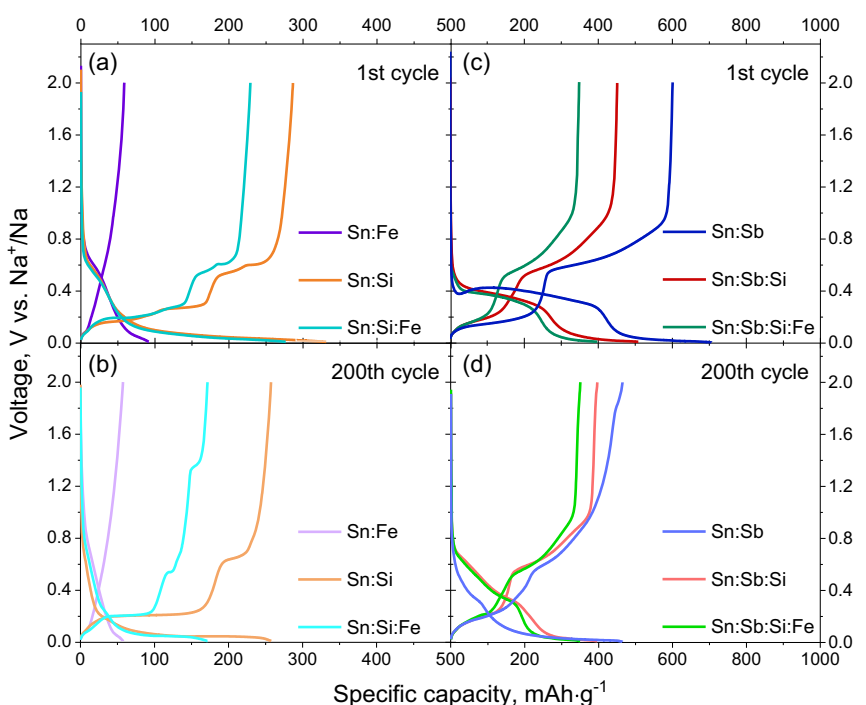


Figure 3. Comparison of the voltage profiles of the 1st and 200th cycles for alloys containing a,b) Sn (Sn:Fe, Sn:Si, and Sn:Si:Fe) and c,d) SnSb (Sn:Sb, Sn:Sb:Si, and Sn:Sb:Si:Fe). Cells were cycled in half-cell geometry at 0.2 C using 1M NaPF₆ in diglyme as electrolyte.

likely not related to Si activity and is instead caused by electrolyte decomposition. This again indicates that Si is electrochemically inactive in the composites, irrespective of its chemical state (being bound in an IM phase or not). On the other hand, the ternary and quaternary electrodes demonstrate an improved cycle life compared to the binary Sn:Sb electrode, showing that the composite improves the cycling stability. After 200 cycles, the samples still provide 78% and 87% of their original capacity, respectively.

While no clear trend between the different samples and their initial Coulomb efficiencies (ICE) could be identified from the data presented in **Table 3**, values typically ranged between 82% and 89%. The Sn:Fe electrode presented an exception, only providing 61.5% Coulomb efficiency during the first cycle, in line with its overall unfavorable characteristics. The highest values, both close to 90%, were found for the ternary and quaternary SnSb-based electrodes, further indicating their improved stability as compared to the other compositions.

Differential capacity plots of the different electrodes are compared in **Figure 4a-f**. As it can be seen from the voltage profiles discussed earlier, the electrochemical behavior of alloys containing both Sn and Sb as active components differs significantly from that of Sn-based materials. For a sample such as Sn:Fe (Figure 4a), no significant electrochemical processes can be observed following the initial sodiation, most likely due to the low amount of active material, such as Sn, being present in the sample to participate in alloying with Na. As for the subsequent Sn-based samples, Sn:Si and Sn:Si:Fe demonstrate the typical multistep sodiation/desodiation processes indicative of an alloying reaction with ball-milled Sn.^[27] For comparison, S3 in the Supporting Information shows the differential capacity plots for electrodes containing only Sn. The voltages of the main sodiation peaks (0.16, 0.27, 0.53, and 0.65 V) correspond well with those observed for both Sn:Si and Sn:Si:Fe, indicating that the redox activity of the composites is due to Sn. As there is a compositional influence over the Na-Sn alloying kinetics, initial charge/discharge cycles of these materials show slight shifts in the peak positions of the relevant alloying steps. However, by the 100th cycle, both samples see the peak positions aligning. This indicates that after initial activation cycles, the general alloying mechanism between Sn:Si and Sn:Si:Fe remains identical.

Findings related to SnSb-based alloy electrodes are presented through the differential capacity plots featured in **Figure 4d-f**. Detection of the formed SnSb alloy is confirmed by the presence of the typical broad sodiation peak around 0.3 V and the desodiation peak at 0.6 V.^[58] No differing features are observed for any of the three samples, indicating that the electrochemistry for samples containing both Sn and Sb in equal ratios always

follows the same pattern. This consistency also suggests that elements such as Si and Fe are redox-inactive during cycling, as no standout features can be discerned between the sample containing only SnSb and those with more elements in the composition. Overall, the derivative plots further support that neither Si nor the different Fe–Si IM phases have any effect on the alloying reactions of Sn and SnSb. They do, however, provide a matrix effect which leads to better rate capability and cycle life as discussed in the next section.

2.4. Electrochemical Properties: Rate Tests and Cycle Life

A rate capability comparison of the different electrodes between 0.1 and 30 C is shown in **Figure 5a**. Results obtained for SnSb demonstrate a significant loss of capacity already at 0.2 C, with values dropping from 360 to 300 mAh g⁻¹. The capacity further decreases with rising currents, reaching values close to 0 at 2 C. This decrease is a kinetic effect, as evidenced by the fact that the capacity recovers when reapplying the initial current of 0.1 C. In fact, the capacity even exceeds the original value, indicating that the electrode is undergoing some activation cycles. Such behavior is not uncommon for conversion reactions, and the increase in capacity values during the rate test at 0.5 and 1 C can be seen as an indication of this (activation cycles for some of the samples can also be seen in the cycle life data in **Figure 5b**). Comparing the results of the binary electrode with the multicomponent alloys, it can be seen that the rate capability is improved by the additional elements. Significantly lower capacity values are delivered by the Sn:Si:Fe alloy, as the addition of Si and Fe leads to a weight penalty. However, its capacity retention compared to other materials proves to be unparalleled, as in the current density range between 0.1 and 1 C, the capacity only decreases by 57 mAh g⁻¹, corresponding to ≈20% of the initial value, excluding the losses due to SEI formation. Even at currents as high as 30 C, the sample still delivers 20 mAh g⁻¹ before returning to its original capacity of around 250 mAh g⁻¹ when the current is again reduced to 0.1 C. This supports the hypothesis of a Si–Fe matrix effect, which buffers the volume changes of the active phases during cycling and supports the electronic wiring between the particles. **Figure S4** (Supporting Information) compares the rate performance of the Sn:Si and Sn:Si:Fe samples as multicomponent Sn-based alloys. In both cases, favorable stability at different rates between 0.1 and 30 C was obtained.

Of all the compositions tested, the Sn:Sb:Si (1:1:1) electrode shows the best compromise between capacity and rate performance, with values of 340 mAh g⁻¹ at 1 C and 480 mAh g⁻¹ at 0.1 C at the end of the rate test. In an attempt to further optimize

Table 3. ICE values of synthesized alloys calculated from the first cycle specific capacity values.

Alloy composition mass ratio	Sn:Sb 1:1	Sn:Si 1:1	Sn:Fe 1:1	Sn:Si:Fe 1:1:1	Sn:Sb:Si 1:1:1	Sn:Sb:Si:Fe 1:1:1:1
Initial discharge capacity [mAh g ⁻¹]	706	331	92	277	508	397
Initial charge capacity [mAh g ⁻¹]	596	287	56	228	450	348
ICE [%]	84.4	86.7	61.5	82	88.5	87.7

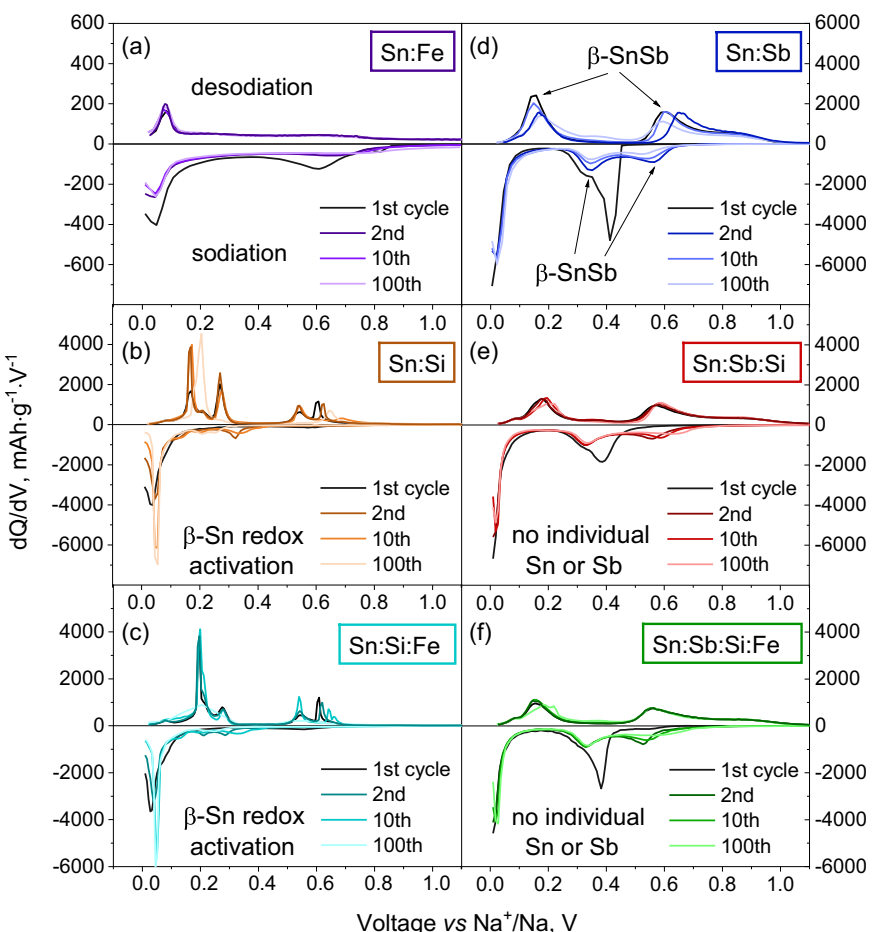


Figure 4. dQ/dV plots of selected cycles for synthesized alloys containing a–c) Sn (Sn:Fe, Sn:Si, and Sn:Si:Fe) and SnSb d–f) (Sn:Sb, Sn:Sb:Si, and Sn:Sb:Si:Fe). Cells were cycled in half-cell geometry at 0.2 C with 1M NaPF_6 in diglyme as electrolyte.

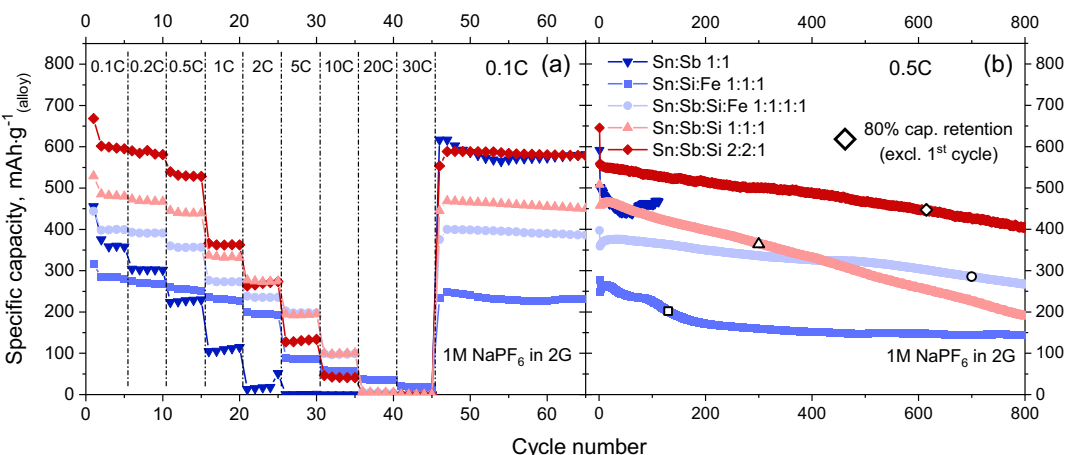


Figure 5. a) Rate capability test between 0.1 and 30C and b) long-term cycling performance at 0.5 C of synthesized alloys Sn:Sb, Sn:Si:Fe, Sn:Sb:Si:Fe, and Sn:Sb:Si (1:1:1 and 2:2:1). The graph also highlights the cycle when capacity retention of 80% is reached (calculation excluding the first cycle). Samples were cycled in half-cells with sodium as the counter electrode.

the composition, the ratio between the elements was changed in order to reduce the amount of inactive Si. The results for the Sn:Sb:Si (2:2:1) electrode are also displayed in the graph and show values of 364 mAh g^{-1} at 1 C and 600 mAh g^{-1} at 0.1 C at the end of the rate test. In fact, the latter value is very close to the

theoretical capacity value of 603 mAh g^{-1} . This shows that by further careful tuning of the electrode composition, optimization of the electrode properties is possible.

Figure 5b demonstrates the capacity variation over 800 charge/discharge cycles at 0.5 C for the different electrodes.

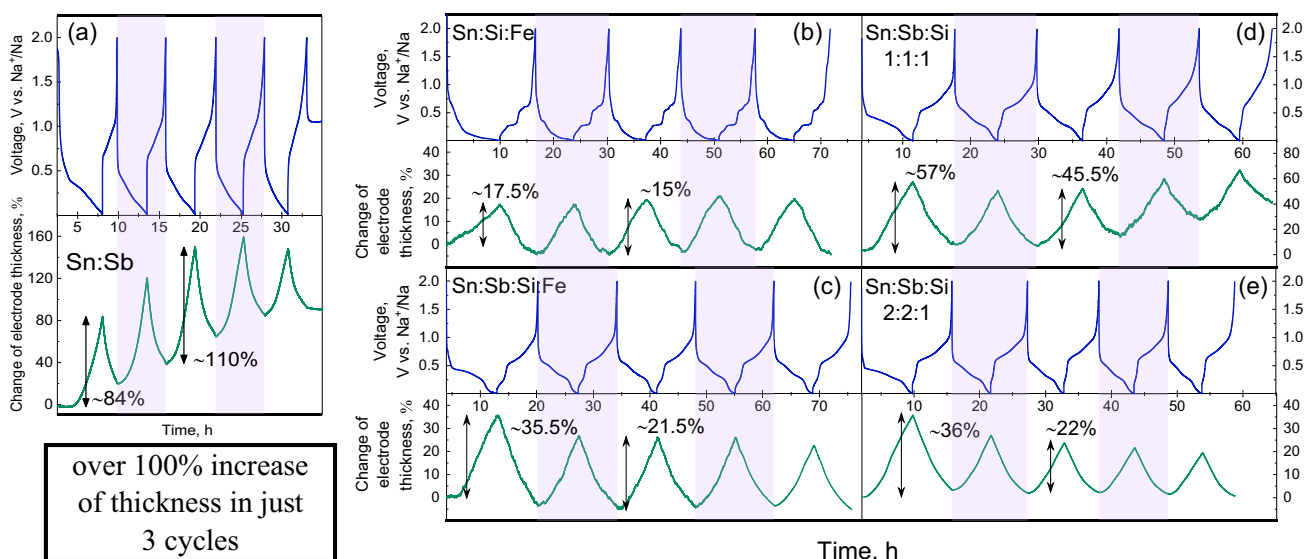


Figure 6. Results from operando ECD inside a climate chamber at 25 °C over five consecutive cycles at constant current 0.1 C with 1 M NaPF₆ in diglyme as electrolyte for a) Sn:Sb, b) Sn:Si:Fe, c) Sn:Sb:Si:Fe, and d,e) Sn:Sb:Si (1:1:1 and 2:2:1).

With the exception of SnSb, all compositions can be cycled over 800 cycles but show differences in capacity and capacity fade rate. The graph also highlights the cycle at which the capacity drops to 80% compared to the second cycle. Despite several attempts, it was not possible to cycle the SnSb electrode at the 0.2 C-rate for more than 111 cycles. The electrode with the lowest capacity (Sn:Si:Fe) shows a strong fading within the first cycles but remains very stable afterward, losing only 27 mAh g⁻¹ between the 200th and 800th cycles. The highest initial capacity values are observed for the Sn:Sb:Si alloys. When excluding the first cycle, they reach values of 457 and 560 mAh g⁻¹ for the 1:1:1 and 2:2:1 weight ratios, respectively. It is unclear at this stage why the latter composition shows an even better cycle life stability, with the 80% criteria not being reached until the 615th cycle. Overall, however, the benefits of using multicomponent alloys to tune the capacity and cycle life behavior are evident. The best cycle life stability was achieved with the quaternary composition Sn:Sb:Si:Fe, reaching the 80% criteria only after 700 cycles. Long-term cycling data for Sn and Sb electrodes is shown in Figure S5 (Supporting Information) for comparison. Note that the poor cycle life for Sb is due to its dissolution in the electrolyte used.^[29] Coulomb efficiencies of the cycles in Figure 5b are presented in Figure S6 (Supporting Information) and show values close to 100% (after the 1st cycle).

2.5. Operando Electrochemical Dilatometry

Since volume expansion is one of the main reasons why alloying anodes experience performance decline over short cycling periods, operando measurements detailing the volume changes during sodiation/desodiation ("breathing") were performed using ECD.^[72] **Figure 6** shows voltage profiles and thickness changes for the different electrodes over the first five charge/discharge cycles. It can be seen that the composition of the electrodes has a strong influence on the degree of electrode breathing

(results for the pure Sn electrode are not included, as the cycling was unstable compared to the other electrodes). Figure 6a provides context for the rapid decline in capacity exhibited by SnSb-only electrodes. Next to severe breathing in excess of 100%, there is also a notable increase in electrode thickness during the early cycles. Both factors are likely to be major contributors to the poor cycle life, as they may lead to particle cracking and contact loss. In contrast, the multicomponent electrodes exhibit much smaller changes. These electrodes breathe between 15% and 57%, and only minor shifts are observed for some of the samples. The smallest thickness change can be observed for Sn:Si:Fe, further decreasing as charge/discharge continues. This may provide an explanation for the high cycling stability that is characteristic of this material. Creating a matrix of both Si and Fe that acts as a buffer mitigates the particle expansion of Sn and results in a near-constant breathing of the anode after initial cycles, improving the overall performance. Although Sn:Sb:Si (1:1:1) exhibits a greater volume expansion compared to both Sn:Sb:Si (2:2:1) and Sn:Sb:Si:Fe, the overall trend remains the same with the volume expansion decreasing by 12–14% after the initial two cycles and continuing on a downward trajectory. These measurements provide clear evidence of the matrix effect, that is, while the additional elements cause a weight penalty, they are able to buffer the volume expansion and therefore enable improved cycling.

3. Conclusion

This study analyzed the possible activation of Si for Na storage as anode material for SIBs. For this, a series of multicomponent alloys consisting of Si, Sn, Sb and Fe were prepared by high energy ball milling. Morphology, phase composition, charge/discharge behavior at different rates, as well as long-term cycling were investigated. The ball milling method produced composites with average particle/agglomerate sizes between 0.5 and 10 µm

and a macroscopically homogeneous elemental distribution. Locally, however, mixing of the different elements led to a variety of IMs. XRD revealed that mixtures of Sn and Sb always led to the SnSb IM and that Si favored alloying with Fe instead of Sn.

The electrochemical results indicated that none of the compositions showed capacity values that would point to electrochemical activity of Si. The measured capacity values were all within the range of what was expected for Sn or SnSb. The voltage profiles also did not provide any indication of Si being redox-active. This led to the conclusion that Si was redox-inactive in all cases despite the high-energy ball milling process producing a variety of phase mixtures and IMs. Nevertheless, Si was found to play a vital role as a structural stabilizer. While there was a weight penalty associated with the addition of redox-inactive Si and Fe, there was a dual benefit as well. On the one hand, the approach enabled high active material utilization close to the theoretical capacity; on the other hand, cycle life and rate performance were also improved. The best compromise between capacity, cycle life, and rate performance was found for Sn:Sb:Si composites with weight ratios of 1:1:1 and 2:2:1. For the latter composition, a discharge capacity of 406 mAh g⁻¹ was reached even after 600 cycles. The improvement in electrode properties was rationalized by operando ECD, which showed a significantly reduced degree of electrode breathing for the multicomponent electrodes compared to the SnSb reference.

Overall, the study showed that the properties of metal anodes for Na-ion batteries can be tailored by mixing redox-active metals (Sn, Sb) and redox-inactive structural stabilizers (Si, Fe), which aligns with findings presented in previous literature.

4. Experimental Section

Materials Synthesis

Synthesis was performed by high-energy planetary ball milling using a Fritsch Pulverisette 7 premium line ball mill and two 80 µL zirconium oxide (ZrO_2) grinding bowls. Crystalline powders of Si (99 + %), Sn (99.8%), Sb (99.5%), and Fe (99 + %) were purchased from Alfa Aesar. XRD patterns recorded for the commercial powders are provided in Figure S1 in the Supporting Information. Depending on the required composition and weight ratios, the powders were combined in grinding bowls inside an argon-filled glovebox. Zirconium oxide grinding balls (10 mm Ø) (Sigmund Lindner GmbH) were then added to the bowls at a weight ratio of 1:20 powder-to-balls. The grinding bowls were then removed from the glovebox and placed into the ball mill. Grinding parameters were set at an intensity of 650 rpm, with the active-to-break ratio being 1:4 for 99 cycles. The resulting powders were removed from the grinding bowls outside the glovebox, weighed, and ground with a mortar and pestle to ensure homogeneity.

Electrode Preparation

Slurries were prepared containing 70 wt% of the ball-milled powder, 20 wt% conductive additive SuperP (MTI Corp.), and 10 wt% binder. The binder was chosen to be an aqueous solution (0.025 g ml⁻¹) containing carboxymethyl cellulose (CMC, MTI Corp.) and styrene butadiene rubber (SBR, MTI Corp.) in a 1:1 weight ratio. Slurries were mixed using a planetary centrifugal mixer (ARE-310, U.S.A. Inc.) with the mixing intensity set to 2000 rpm. Mixing was performed in 3–5 min

intervals with the addition of a total of 2 µL of deionized water during the breaks to achieve the desired viscosity. The slurries were then applied onto carbon-coated copper foil (MTI Corp.) using a doctor blade with a set application thickness of 300 µm. After drying the films, 12 and 10 mm Ø electrodes were punched and dried at 80 °C under vacuum for 6 h and transferred into the glovebox. 1 M hexafluorophosphate (NaPF_6 , >99%, Alfa Aesar) in diglyme (2G, Sigma Aldrich, dried over a 4 Å molecular sieve) was used as electrolyte. CR 2032 coin half-cells (MTI Corp.) were assembled using the prepared electrodes, 100 µL of electrolyte, and two 16 mm Ø separators (Whatman). 12 mm Ø sodium electrodes (BASF) were used as counter electrodes.

Characterization

Galvanostatic cycling with potential limitation was performed on a NEWARE multichannel battery test system in the potential range between 0.01 and 2.0 V versus Na^+/Na . The currents were calculated to correspond to the C-rate of 0.1 C charge/discharge time while taking into account the theoretical capacities of the active elements Sn and Sb (847 and 660 mAh g⁻¹, respectively). It followed that the currents applied at 0.1 C were 85 mA g⁻¹ for Sn-based compounds and 75 mA g⁻¹ for compounds containing both Sn and Sb. It should also be noted that currents were calculated using only the mass loading of active elements present in the composition based on the intended ratio. Theoretical areal capacities ranged from 0.95 to 2.75 mAh cm⁻² (assuming only Sn and Sb are redox-active). Rate capability testing was performed in the same voltage window with C-rates of 0.1, 0.2, 0.5, 1, 2, 5, 10, 20, 30 C, and then 0.1 C again. Operando ECD measurements were performed on an ECD-3-nano cell device from EL-CELL in a temperature-controlled chamber at 25 °C. Working electrodes of 10 mm Ø were used. 250 µL of electrolyte (1 M NaPF_6 in 2G) was used along with sodium counter and reference electrodes in a three-electrode setup.

Phase identification for the obtained materials was performed by powder XRD (D2-phaser, Bruker) using Cu-Kα radiation (30 kV, 10 mA). Measurements were carried out in the range between 20° and 80° with a step of 0.02°. For the morphology, SEM was conducted using Zeiss Merlin (at Helmholtz-Zentrum Berlin (HZB) in Adlershof) at 20–30 kV accelerating voltage. Raman spectroscopy was performed using a Renishaw inVia confocal Raman microscope with a 532 nm laser. Measurements were made at 0.5% laser power and 3 accumulations with 10 s exposure time.

Acknowledgements

P.A. acknowledges support from the German Research Foundation (grant no. 444658496). The authors would like to acknowledge the electron microscopy corelab (CCMS) of Helmholtz-Zentrum Berlin (HZB) for allocation of the scanning electron microscope measurement and M.Sc. M. Exner for assisting with Raman spectroscopy measurements. The authors also thank BASF SE for providing high-purity Na metal.

Open Access funding enabled and organized by Projekt DEAL.

Conflict of Interest

The authors declare no conflict of interest.

Data Availability Statement

Research data are not shared.

Keywords: alloys · ball milling · intermetallic phases · silicon · sodium-ion batteries

- [1] K. Chayambuka, G. Mulder, D. L. Danilov, P. H. Notten, *Adv. Energy Mater.* **2018**, *8*, 1800079.
- [2] F. Arshad, J. Lin, N. Manurkar, E. Fan, A. Ahmad, F. Wu, R. Chen, L. Li, *Resour. Conserv. Recycl.* **2022**, *180*, 106164.
- [3] P. K. Nayak, L. Yang, W. Brehm, P. Adelhelm, *Angew. Chem., Int. Ed.* **2018**, *57*, 102.
- [4] A. Eftekhari, D. W. Kim, *J. Power Sources* **2018**, *395*, 336.
- [5] T. Perveen, M. Siddiq, N. Shahzad, R. Ihsan, A. Ahmad, M. I. Shahzad, *Renewable Sustainable Energy Rev.* **2020**, *119*, 109549.
- [6] V. Palomares, M. Casas-Cabanas, E. Castillo-Martínez, M. H. Han, T. Rojo, *Energy Environ. Sci.* **2013**, *6*, 2312.
- [7] C. Vaalma, D. Buchholz, M. Weil, S. Passerini, *Nat. Rev. Mater.* **2018**, *3*, 1.
- [8] M. Walter, M. V. Kovalenko, K. V. Kravchyk, *New J. Chem.* **2020**, *44*, 1677.
- [9] Z. Dai, U. Mani, H. T. Tan, Q. Yan, *Small Methods* **2017**, *1*, 1700098.
- [10] Y. Kim, K. H. Ha, S. M. Oh, K. T. Lee, *Chem.-A Eur. J.* **2014**, *20*, 11980.
- [11] W. Zheng, G. Liang, Q. Liu, J. Li, J. A. Yuwono, S. Zhang, V. K. Peterson, Z. Guo, *Joule* **2023**, *7*, 2732.
- [12] X. Pu, H. Wang, D. Zhao, H. Yang, X. Ai, S. Cao, Z. Chen, Y. Cao, *Small* **2019**, *15*, 1805427.
- [13] R. Zhao, N. Sun, B. Xu, *Small Struct.* **2021**, *2*, 2100132.
- [14] E. Goikolea, V. Palomares, S. Wang, I. R. de Larramendi, X. Guo, G. Wang, T. Rojo, *Adv. Energy Mater.* **2020**, *10*, 2002055.
- [15] H. Tan, D. Chen, X. Rui, Y. Yu, *Adv. Funct. Mater.* **2019**, *29*, 1808745.
- [16] S. M. Zheng, Y. R. Tian, Y. X. Liu, S. Wang, C. Q. Hu, B. Wang, K. M. Wang, *Rare Met.* **2021**, *40*, 272.
- [17] K. Song, C. Liu, L. Mi, S. Chou, W. Chen, C. Shen, *Small* **2021**, *17*, 1903194.
- [18] P. Zheng, J. Sun, H. Liu, R. Wang, C. Liu, Y. Zhao, J. Li, Y. Zheng, X. Rui, *Batter. Supercaps* **2023**, *6*, e202200481.
- [19] V. L. Chevrier, G. Ceder, *J. Electrochem. Soc.* **2011**, *158*, A1011.
- [20] S. Qiao, Q. Zhou, M. Ma, H. K. Liu, S. X. Dou, S. Chong, *ACS Nano* **2023**, *17*, 11220.
- [21] I. Hasa, S. Mariyappan, D. Saurel, P. Adelhelm, A. Y. Koposov, C. Masquelier, L. Croguennec, M. Casas-Cabanas, *J. Power Sources* **2021**, *482*, 228872.
- [22] L. Zhang, X. Hu, C. Chen, H. Guo, X. Liu, G. Xu, H. Zhong, S. Cheng, P. Wu, J. Meng, Y. Huang, S. Dou, H. Liu, *Adv. Mater.* **2018**, *29*, 1604708.
- [23] H. Q. Wang, Y. X. Zhao, L. Gou, L. Y. Wang, M. Wang, Y. Li, S. L. Hu, *Rare Met.* **2022**, *41*, 1626.
- [24] S. Huang, L. Liu, Y. Zheng, Y. Wang, D. Kong, Y. Zhang, Y. Shi, L. Zhang, O. G. Schmidt, H. Y. Yang, *Adv. Mater.* **2018**, *30*, 1706637.
- [25] Y. Xu, E. Swaans, S. Basak, H. W. Zandbergen, D. M. Borsa, F. M. Mulder, *Adv. Energy Mater.* **2016**, *6*, 1501436.
- [26] W. T. Jing, C. C. Yang, Q. Jiang, *J. Mater. Chem. A* **2020**, *8*, 2913.
- [27] T. Palanisvam, M. Goktas, B. Anothumakkool, Y. N. Sun, R. Schmuck, L. Zhao, B.-H. Han, M. Winter, P. Adelhelm, *Adv. Funct. Mater.* **2019**, *29*, 1900790.
- [28] T. Palanisvam, B. Babu, H. Moon, I. Hasa, A. L. Santhosha, M. Goktas, Y.-N. Sun, L. Zhao, B.-H. Han, S. Passerini, A. Balducci, P. Adelhelm, *Batter. Supercaps* **2021**, *4*, 173.
- [29] W. Brehm, J. R. Buchheim, P. Adelhelm, *Energy Technol.* **2019**, *7*, 1900389.
- [30] M. He, M. Walter, K. V. Kravchyk, R. Erni, R. Widmer, M. V. Kovalenko, *Nanoscale* **2015**, *7*, 455.
- [31] J. Barker, F. Coowar, J. Fullenwarth, L. Monconduit, *J. Power Sources* **2022**, *541*, 231702.
- [32] W. P. Kalisvaart, B. C. Olsen, E. J. Luber, J. M. Buriak, *ACS Appl. Energy Mater.* **2019**, *2*, 2205.
- [33] S. Y. Sayed, W. P. Kalisvaart, E. J. Luber, B. C. Olsen, J. M. Buriak, *ACS Appl. Energy Mater.* **2020**, *3*, 9950.
- [34] J. Qian, Y. Xiong, Y. Cao, X. Ai, H. Yang, *Nano Lett.* **2014**, *14*, 1865.
- [35] T. Palanisvam, C. Mukundan, I. Hasa, A. L. Santhosha, M. Goktas, H. Moon, M. Rutter, R. Schmuck, K. Pollok, F. Langenhorst, M. Winter, S. Passerini, P. Adelhelm, *Adv. Funct. Mater.* **2020**, *30*, 2004798.
- [36] L. O. Vogt, C. Villevieille, *J. Mater. Chem. A* **2016**, *4*, 19116.
- [37] L. O. Vogt, C. Villevieille, *J. Mater. Chem. A* **2017**, *5*, 3865.
- [38] S. Guo, Y. Feng, L. Wang, Y. Jiang, Y. Yu, X. Hu, *Small* **2021**, *17*, 2005248.
- [39] Y. Tian, Y. An, B. Zhang, *Adv. Energy Mater.* **2023**, *13*, 2300123.
- [40] W. Zhang, M. Dahbi, S. Komaba, *Curr. Opin. Chem. Eng.* **2016**, *13*, 36.
- [41] Q. Yao, Y. Zhu, C. Zheng, N. Wang, D. Wang, F. Tian, Z. Bai, J. Yang, Y. Qian, S. Dou, *Adv. Energy Mater.* **2023**, *13*, 2202939.
- [42] B. Zhang, G. Rousse, D. Foix, R. Dugas, D. A. Dalla Corte, J. M. Tarascon, *Adv. Mater.* **2016**, *28*, 9824.
- [43] J. M. Liang, L. J. Zhang, L. D. G. Xi, J. Kang, *Rare Met.* **2020**, *39*, 1005.
- [44] S. Liang, Y. J. Cheng, J. Zhu, Y. Xia, P. Müller-Buschbaum, *Small Methods* **2020**, *4*, 2000218.
- [45] A. Darwiche, M. T. Sougrati, B. Fraisse, L. Stievano, L. Monconduit, *Electrochem. Commun.* **2013**, *32*, 18.
- [46] D. Zhou, M. Slater, D. Kim, E. Lee, J. Jorne, C. Johnson, *ECS Trans.* **2014**, *58*, 59.
- [47] J. Qin, T. Wang, D. Liu, E. Liu, N. Zhao, C. Shi, F. He, L. Ma, C. He, *Adv. Mater.* **2018**, *30*, 1704670.
- [48] H. Jia, M. Dirican, C. Aksu, N. Sun, C. Chen, J. Zhu, P. Zhu, C. Yan, Y. Li, Y. Ge, J. Guo, X. Zhang, *J. Colloid Interface Sci.* **2019**, *536*, 655.
- [49] D. Tan, P. Chen, G. Wang, G. Chen, T. Pietsch, E. Brunner, T. Doert, M. Ruck, *RSC Adv.* **2020**, *10*, 22250.
- [50] C. Li, Y. R. Pei, M. Zhao, C. C. Yang, Q. Jiang, *Chem. Eng. J.* **2021**, *420*, 129617.
- [51] X. Shi, W. Liu, D. Zhang, C. Wang, J. Zhao, X. Wang, B. Chen, L. Chang, Y. Cheng, L. Wang, *Chem. Eng. J.* **2022**, *431*, 134318.
- [52] J. Li, J. Pu, Z. Liu, J. Wang, W. Wu, H. Zhang, H. Ma, *ACS Appl. Mater. Interfaces* **2017**, *9*, 25250.
- [53] A. Verdianto, H. Lim, J. G. Kang, S. O. Kim, *Int. J. Energy Res.* **2022**, *46*, 4267.
- [54] A. Verdianto, H. Lim, J. Park, S. O. Kim, *J. Alloys Compd.* **2023**, *942*, 168950.
- [55] J. Ma, A. L. Prieto, *Chem. Commun.* **2019**, *55*, 6938.
- [56] L. Elias, M. Bhar, S. Ghosh, S. K. Martha, *Ionics* **2022**, *28*, 2759.
- [57] H. Xie, X. Tan, E. J. Luber, B. C. Olsen, W. P. Kalisvaart, K. L. Jungjohann, D. Mitlin, J. M. Buriak, *ACS Energy Lett.* **2018**, *3*, 1670.
- [58] W. P. Kalisvaart, H. Xie, B. C. Olsen, E. J. Luber, J. M. Buriak, *ACS Appl. Energy Mater.* **2019**, *2*, 5133.
- [59] H. Xie, W. P. Kalisvaart, B. C. Olsen, E. J. Luber, D. Mitlin, J. M. Buriak, *J. Mater. Chem. A* **2017**, *5*, 9661.
- [60] B. Farbod, K. Cui, W. P. Kalisvaart, M. Kupsta, B. Zahiri, A. Kohandehghan, E. M. Lotfabad, Z. Li, E. J. Luber, D. Mitlin, *ACS Nano* **2014**, *8*, 4415.
- [61] E. Edison, S. Sreejith, H. Ren, C. T. Lim, S. Madhavi, *J. Mater. Chem. A* **2019**, *7*, 14145.
- [62] E. Edison, S. Sreejith, S. Madhavi, *ACS Appl. Mater. Interfaces* **2017**, *9*, 39399.
- [63] P. C. Patel, S. Awasthi, P. K. Mishra, P. Lakharwal, J. Kashyap, *Energy Fuels* **2023**, *37*, 16062.
- [64] F. Sato, T. Honma, T. Komatsu, A. A. B. Kaharudin, T. Homma, S. Ito, *J. Alloys Compd.* **2023**, *947*, 169576.
- [65] T. B. Reddy, *Linden's Handbook of Batteries*, 4th ed., McGraw-Hill, New York 2011.
- [66] A. D. W. Todd, P. P. Ferguson, M. D. Fleischauer, J. R. Dahn, *Int. J. Energy Res.* **2010**, *34*, 535.
- [67] Y. Li, F. Wu, Y. Li, M. Liu, X. Feng, Y. Bai, C. Wu, *Chem. Eng. Soc. Rev.* **2022**, *51*, 4484.
- [68] F. Klein, B. Jache, A. Bhide, P. Adelhelm, *Phys. Chem. Chem. Phys.* **2013**, *15*, 15876.
- [69] M. K. Jangid, A. S. Lakhnot, A. Vemulapally, F. J. Sonia, S. Sinha, R. O. Dusane, A. Mukhopadhyay, *J. Mater. Chem. A* **2018**, *6*, 3422.
- [70] M. M. Abed, A. Kiani, *Results Mater.* **2020**, *8*, 100157.
- [71] L. D. Ellis, T. D. Hatchard, M. N. Obrovac, *J. Electrochem. Soc.* **2012**, *159*, A1801.
- [72] I. Escher, M. Hahn, G. A. Ferrero, P. Adelhelm, *Energy Technol.* **2022**, *10*, 2101120.
- [73] C. Schmetterer, J. Polt, H. Flandorfer, *J. Alloys Compd.* **2018**, *743*, 523.
- [74] R. W. Olesinski, G. J. Abbaschian, *Bull. Alloy Phase Diagr.* **1984**, *5*, 273.
- [75] W. B. Park, M. C. Bernhard, P. Presoly, Y. B. Kang, *J. Mater. Inform.* **2023**, *3*, 5.
- [76] A. Mostafa, M. Medraj, *Materials* **2017**, *10*, 676.
- [77] B. Pei, B. Björkman, B. Sundman, B. Jansson, *Calphad* **1995**, *19*, 1.
- [78] Y. Liu, X. Xu, C. Wu, H. Peng, J. Wang, X. Su, *Calphad* **2018**, *63*, 82.
- [79] J. Lacaze, B. Sundman, *Metall. Trans. A* **1991**, *22*, 2211.

Manuscript received: October 29, 2024

Revised manuscript received: March 9, 2025

Version of record online: March 14, 2025